IMA Journal of Applied Mathematics (2021) **86**, 1094–1111
https://doi.org/10.1093/imamat/hxab028
Advance Access publication on 17 August 2021

Curvature effects and radial homoclinic snaking

Damià Gomila*
IFISC (CSIC-UIB), Instituto de Física Interdisciplinar y Sistemas Complejos, E-07122 Palma de Mallorca, Spain
*Corresponding author: damia@ifisc.uib-csic.es

and

Edgar Knobloch
Department of Physics, University of California at Berkeley, Berkeley, CA 94720, USA

[Received on 16 October 2020; revised on 7 May 2021; accepted on 10 June 2021]

In this work, we revisit some general results on the dynamics of circular fronts between homogeneous states and the formation of localized structures in two dimensions (2D). We show how the bifurcation diagram of axisymmetric structures localized in radius fits within the framework of collapsed homoclinic snaking. In 2D, owing to curvature effects, the collapse of the snaking structure follows a different scaling that is determined by the so-called nucleation radius. Moreover, in the case of fronts between two symmetry-related states, the precise point in parameter space to which radial snaking collapses is not a 'Maxwell' point but is determined by the curvature-driven dynamics only. In this case, the snaking collapses to a 'zero surface tension' point. Near this point, the breaking of symmetry between the homogeneous states tilts the snaking diagram. A different scaling law is found for the collapse of the snaking curve in each case. Curvature effects on axisymmetric localized states with internal structure are also discussed, as are cellular structures separated from a homogeneous state by a circular front. While some of these results are well understood in terms of curvature-driven dynamics and front interactions, a proper mathematical description in terms of homoclinic trajectories in a radial spatial dynamics description is lacking.

Keywords: collapsed homoclinic snaking; localized structures; curvature-driven front dynamics.

1. Introduction

The formation of spatially localized structures (LSs) is ubiquitous in systems driven out of equilibrium. Such structures have been observed in a large variety of physical, chemical and biological systems (Akhmediev & Ankiewicz, 2008; Purwins *et al.*, 2010). As a highly nonlinear phenomenon, they are difficult to tackle from a mathematical point of view. Physicists often approach this type of problem by focusing on the linear and nonlinear mechanisms at play, whose interaction leads to a self-sustained localized nonlinear state called an LS or, more generally, a dissipative soliton. While this approach has provided a compelling explanation for the existence and stability of LSs in many systems, it was the proper mathematical analysis of the spatial dynamical systems describing stationary solutions of partial differential equations (PDEs) (Coullet *et al.*, 2000; Woods & Champneys, 1999) that revealed the bifurcation structure of LSs and led to the notion of what is now known as homoclinic snaking (Woods & Champneys, 1999). In this phenomenon, homoclinic states representing LSs embedded in a background state accumulate on a heteroclinic cycle corresponding to back-to-back fronts between a homogeneous state and, typically, a spatially periodic state, as exemplified by the Swift–Hohenberg equation (Burke & Knobloch, 2007). When the two states involved in the heteroclinic cycle are both

homogeneous, the resulting LS bifurcation diagram may still snake, provided the spatial eigenvalues of one or both of the competing states are complex, but the parameter region where LSs exist shrinks as they become broader, tending to a single point as their width diverges. The resulting bifurcation diagram is known as collapsed snaking (Burke & Knobloch, 2007).

In the spatial dynamical system describing stationary solutions of a PDE, spatially extended coordinates play the role of 'time', in what is known as a spatial dynamics description. Such a theory is well established in one spatial dimension (1D) but becomes problematic in 2D. However, for axisymmetric states, the radial coordinate remains a good time-like coordinate although the resulting dynamical system is now non-autonomous. This approach has been used to describe axisymmetric solutions resulting from the coexistence between homogeneous and periodic solutions (Avitabile *et al.*, 2010; Bramburger *et al.*, 2019; Faye *et al.*, 2013; Glasner & Lindsay, 2013; Lloyd & Sandstede, 2009; Ma & Knobloch, 2016; McCalla & Sandstede, 2010). In 2D, the possibility that an interface between two states can bend changes the dynamical properties substantially with respect to the dynamics of a flat interface. This is the case, for instance, of the Gibbs–Thomson or Kelvin effects, whereby the vapour pressure or chemical potential of a solid–liquid or liquid–gas interface changes according to its curvature. As a result, the melting point of small particles occurs, typically, at lower temperatures than the bulk (Perez, 2005). In contrast, the Kelvin effect describes the reduction of the surface tension of a liquid with increasing curvature of the surface. As a result, the evaporation rate increases for small drops (Lewis, 2006). Such effects are well known in equilibrium thermodynamics and lead to curvature-driven minimization of surface tension energy as described by the Allen–Cahn equation (Allen & Cahn, 1979).

In systems driven out of equilibrium, curvature-driven dynamics does not necessarily minimize any obvious quantity. In general, in systems with two coexisting homogeneous solutions, the curvature typically generates an inward velocity of a circular domain wall, thereby progressively reducing its radius. If the inward driving is not too strong, the interaction between opposite parts of a circular domain through the tails of the front may halt the inwards motion leading to the formation of LSs. This phenomenon has been studied in the Swift–Hohenberg equation (Ouchi & Fujisaka, 1996), as well as in different nonlinear optical systems (Gallego *et al.*, 2000; Oppo *et al.*, 1999, 2001; Staliunas & Sanchez-Morcillo, 1998), where it is responsible for the presence of dark-ring cavity solitons. The curvature-driven force may interact with other driving mechanisms, leading to modified snaking scenarios, as in the forced complex Ginzburg–Landau (FCGL) equation with 1:1 (Ma & Knobloch, 2016) and 2:1 temporal resonance (Gomila *et al.*, 2001, 2004). In the present work, we revisit some results from the physics literature on axisymmetric LSs in 2D in systems with bistability between two homogeneous or structured states from the point of view of radial spatial dynamics and discuss some of their properties together with a number of open questions.

The paper is organized as follows: in Section 2, we review the general theory of front motion and pinning. In Section 3, we describe the dynamical regimes and LSs predicted by the general theory and compare the results with specific models. In Section 4, we discuss curvature effects in localized states with internal structure. The paper ends in Section 5 with some concluding remarks.

2. Dynamics of circular fronts between homogeneous states

Following Gomila *et al.* (2001), we consider a system described by N real fields Ψ_i, with $i = 1, 2..., N$, whose dynamical evolution in two spatial dimensions follows a set of PDEs which read, in vectorial form,

$$\partial_t \vec{\Psi} = \underline{D} \cdot \nabla^2 \vec{\Psi} + \vec{W}(\vec{\Psi}, p)\,, \tag{2.1}$$

where the matrix $\underline{D}$ describes the spatial coupling, $\nabla^2 \equiv \partial_x^2 + \partial_y^2$, $\vec{W}$ is a local nonlinear function of the fields and p is a control parameter. Equation (2.1) is posed in the plane and invariant under translations. This description includes any N-field reaction–diffusion system but also purely diffractive optical systems. In the latter case, the complex amplitude field is written in its real and imaginary parts, and the diffractive coupling leads to a matrix $\underline{D}$ with non-zero terms only in off-diagonal positions. Both types of system are well known for supporting localized states (Akhmediev & Ankiewicz, 2008). If $\vec{\Psi}$ is a scalar and W can be derived from an energy potential, (2.1) corresponds to the well-known Allen–Cahn equation describing curvature-driven minimization of surface tension, leading to a $t^{1/2}$ power law for the domain size growth (Allen & Cahn, 1979; Shen & Yang, 2010).

In this section, we assume that, for certain values of p, (2.1) has two stable homogeneous solutions and that in 1D these solutions are connected by a stable front $\vec{\Psi}_0(x,p)$ moving at velocity $c(p)$. A 1D front (equivalently a flat front in 2D) is stationary in a reference frame moving at velocity c in the direction transverse to the front if $[c(p)\underline{I}\partial_x + \underline{D}\partial_x^2] \cdot \vec{\Psi}_0 + \vec{W}(\vec{\Psi}_0, p) = 0$, where $\underline{I}$ is the identity matrix.

Let $\vec{X}(s,t)$ represent the instantaneous position vector of the front in the $\vec{x} \equiv (x,y)$ plane, where s is the coordinate along the front. It is convenient to define a second coordinate system (r,s) that moves with the front such that $\vec{x} = \vec{X}(s,t) + r\hat{r}(s,t)$, where $\hat{r}$ is a unit vector normal to the curve $\vec{X}$ and the coordinate r is the distance of the point $\vec{x}$ to the front (Meron, 1992). In the moving reference frame, (2.1) becomes

$$\underline{D} \cdot \partial_r^2 \vec{\Psi} + \left[(v+c)\underline{I} + \frac{\kappa}{1+r\kappa}\underline{D} \right] \cdot \partial_r \vec{\Psi} + \frac{\kappa^2}{(1+r\kappa)^2}\underline{D} \cdot \partial_\theta^2 \vec{\Psi} + \vec{W}(\vec{\Psi}, p) = \partial_t \vec{\Psi}\,, \tag{2.2}$$

where $v = \partial_t \vec{X} \cdot \hat{r} - c$ is the (normal) front velocity in excess of c due to the curvature of the front, $\kappa = \nabla \cdot \hat{r}$ is the curvature and $\theta = \kappa s$ is the azimuthal angle. We analyse the dynamics of slightly curved fronts as a perturbation of the flat front $\vec{\Psi}(r,s,t) = \vec{\Psi}_0(r) + \vec{\Psi}_1(r,s,t)$. We assume mild curvature ($\kappa w \ll 1$, where w is the front width), that the fronts are circular ($\partial_\theta^2 \vec{\Psi} = 0$) and that they move largely without changing their profile ($|\partial_t \vec{\Psi}| \ll |\kappa \underline{D} \cdot \partial_r \vec{\Psi}|$). Linearizing around $\vec{\Psi}_0$, we have

$$\underline{M} \cdot \vec{\Psi}_1 = -(v\underline{I} + \kappa \underline{D}) \cdot \partial_r \vec{\Psi}_0\,, \tag{2.3}$$

where $M_{i,j} = c(p) I_{i,j} \partial_r + D_{i,j}\partial_r^2 + \frac{\delta W_i}{\delta \Psi_j}|_{\vec{\Psi}_0, p}$ is the Jacobian of (2.1) evaluated at the flat front $\vec{\Psi}_0$ in the moving reference frame. Owing to the translational invariance of (2.1), the matrix $\underline{M}$ is singular, $\underline{M} \cdot \vec{e}_0 = 0$, where $\vec{e}_0 \equiv \partial_r \vec{\Psi}_0$ is the Goldstone mode. The solvability condition applied to (2.3) leads to $v = -\gamma(p)\kappa$, where

$$\gamma(p) \equiv \frac{1}{\Gamma} \int_{-\infty}^{\infty} \vec{a}_0 \cdot \underline{D} \cdot \vec{e}_0 \, \mathrm{d}r\,, \tag{2.4}$$

with $\Gamma \equiv \int_{-\infty}^{\infty} \vec{a}_0 \cdot \vec{e}_0 \, \mathrm{d}r$ and $\vec{a}_0$ the null mode of $\underline{M}^\dagger$. For a circular structure, κ is the inverse of the radius of curvature R and $\dot{R} = c + v$:

$$\dot{R} = c(p) - \gamma(p)/R\,. \tag{2.5}$$

In systems with two different stable homogeneous states the speed $c(p)$ is in general non-zero and its sign depends on the relative stability of the two asymptotic states. Close to the point where the front between the two states is stationary, a point referred to in general as the 'Maxwell point' by analogy with equilibrium phase transitions, the speed c can be approximated to leading order as $c \approx c_0(p-p_M)$, where c_0 is a constant. Farther away from this point c depends on p nonlinearly but generally takes an O(1) value. In systems with two equivalent competing states, $c = 0$ for all values of p, and the radial velocity is determined by curvature-driven dynamics only. Here, by equivalent, we mean two symmetry-related states of a potential system with identical energy or more generally non-potential systems in which a symmetry forces the front to be always at rest (Ophaus *et al.*, 2021).

In systems with no cross-diffusion and where all fields have the same diffusion constant, $\underline{D} = d\underline{I}$ and the coefficient $\gamma(p)$ takes the constant value d. This situation excludes effects like the Turing instability in reaction–diffusion systems. For a single complex field, no cross-diffusion means that the parameter in front of the Laplacian term is real and, therefore, that diffractive coupling is absent. More generally, in potential systems, γ is related to the strength of the surface tension. In non-potential systems, however, γ cannot be related to a surface energy, although it still plays the role of an effective surface tension. In systems with different diffusion constants for different fields or off-diagonal terms in $\underline{D}$, γ depends in general on p and can in some cases change sign at a critical point $p = p_c$. For positive values of γ (positive surface tension), circular domains shrink to reduce the length of the interface, while for negative values of γ circular domains grow. The latter is typically associated with a modulational instability of the front, as the system tends to increase the length of the interface, leading to labyrinthine patterns. Near this transition, $\gamma = \gamma_0(p - p_c)$ to leading order. Very close to p_c, γ is small and higher order terms in $1/R$ must be taken into account. A weakly nonlinear analysis (Gomila *et al.*, 2001) leads to:

$$\dot{R} = c(p) - \gamma_0(p - p_c)/R + a/R^2 - b/R^3 \,. \tag{2.6}$$

In systems with equivalent states, for symmetry reasons, $a = 0$.

While (2.6) is strictly valid for large R only, as the radius decreases, an interaction between oscillatory tails from opposite parts of the circular front may come into play. Although the resulting interaction force has not been systematically derived, by analogy with the 1D case, one can expect, at least for large R, that the radial force due to the radial oscillations of the front profile as it approaches the homogeneous solution at the center of the domain has the form $f(R) = g\cos(2\beta R)e^{2\alpha R}$ (Coullet *et al.*, 1987), where α and β are the real and imaginary parts, respectively, of the leading eigenvalue of the radial spatial dynamics description of the homogeneous solution at the center of the circular domain. Thus,

$$\dot{R} = c(p) - \gamma(p)/R + a/R^2 - b/R^3 + g\cos(2\beta R)e^{2\alpha R} \,, \tag{2.7}$$

where $c = c_0(p - p_M)$ around $p = p_M$ and $\gamma = \gamma_0(p - p_c)$ around $p = p_c$.

Beyond the usual (local) spatial coupling described by spatial derivatives, some processes are best described by a non-local spatial coupling, described in the models by an integral term. Such non-local interactions can modify some of the terms in (2.7). For instance, in Gelens *et al.* (2010), a large amplification in the interaction strength between two opposite 1D fronts was observed in a non-local version of the Ginzburg–Landau equation, affecting mainly the values of α, β and g. In that work, kernels decaying exponentially or faster with the distance were considered. For a Lorentzian kernel, the non-local effects have an even longer range, introducing modifications in γ_0 or b depending on the

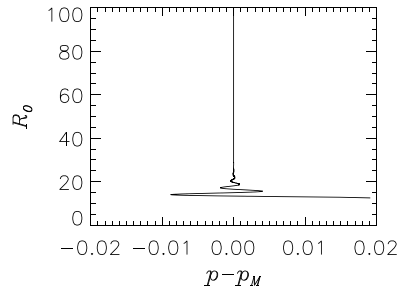

FIG. 1. Stationary distance R_0 as a function of p according (2.7) for the 1D case. Here R_0 must be interpreted as half the distance between back-to-back fronts, i.e. as half the width of the LSs. We take $c_0 = 1$, $\gamma_0 = 0$, $a = 0$, $b = 0$, $g = 10$, $\beta = 1$ and $\alpha = -0.25$.

dimensionality of the system (Fernandez-Oto *et al.*, 2013). In 1D, γ_0 becomes non-zero, leading to the formation of a distinct type of LS. In 2D, non-locality increases considerably the value of b making it O(1).

Equation (2.7) incorporates in a single equation all the mechanisms driving the dynamics of fronts in 2D, and it is the key to interpreting a number of the results found in the literature within the same framework. In particular, in the next section, we analyse different scenarios leading to the formation of LSs depending on the prevailing driving mechanism.

3. Collapsed snaking

Equation (2.7) captures a number of scenarios observed in different physical systems. In this section, we study the main cases.

3.1 *1D collapsed snaking*

For flat fronts, (2.7) reproduces the usual 1D collapsed snaking (Burke & Knobloch, 2007). In this case, R must be interpreted as half the distance between two back-to-back fronts and there are no curvature effects ($\gamma_0 = a = b = 0$). Figure 1 shows a typical collapsed snaking curve. The sections of the curve with positive (negative) slope correspond to stable (unstable) equilibrium points of (2.7).

In the spatial dynamics description, a 'Maxwell point' corresponds to the formation of a heteroclinic cycle between the two competing homogeneous solutions (fixed points of the spatial dynamics). Because of the reversibility property and the fact that the spatial eigenvalues of the fixed points are in general complex, homoclinic orbits corresponding to localized states are created in a series of saddle-node bifurcations that accumulate exponentially at the 'Maxwell point' p_M.

This scenario has been identified in many different physical systems (Lo Jacono *et al.*, 2017; Oza *et al.*, 2014; Parra-Rivas & Fernandez-Oto, 2020; Tseluiko *et al.*, 2014; Tzou *et al.*, 2013). Parra-Rivas *et al.* (2020) show an example in nonlinear optical Kerr resonators. In the latter system collapsed snaking has been observed experimentally by Li *et al.* (2020).

3.2 *Collapsed radial snaking*

In two spatial dimensions, curvature-driven dynamics come into play. Close to the Maxwell point and away from p_c, one can take γ to be positive and O(1) and suppose that it is approximately constant

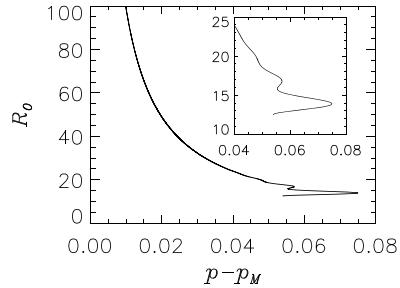

FIG. 2. Stationary radius R_0 as a function of p according (2.7). The inset shows a zoom of the crossover region. Here $c_0 = 1$, $\gamma = 1$, $a = 1$, $b = -1$, $g = 10$, $\beta = 1$ and $\alpha = -0.25$.

for small changes of p around p_M. Since the strength of the interaction between the tails of the fronts decreases exponentially with increasing radius while the curvature effects do so algebraically as $1/R$, for sufficiently large radius the tail interaction becomes negligible with respect to the other terms in (2.7). Moreover, as $\gamma \neq 0$, nonlinear curvature effects do not play a crucial role either. In this case, the outward velocity driven by the distance from p_M ($p > p_M$) can be counteracted by the curvature ($\gamma > 0$), leading to a large stationary radius, known as the nucleation radius, that diverges at $p = p_M$:

$$R_0 = \frac{\gamma}{c_0(p - p_M)}\,. \tag{3.1}$$

Therefore, in contrast to the 1D case, the bifurcation diagram of the LSs collapses 'algebraically' to p_M instead of 'exponentially' (Fig. 2). Note that the resulting equilibrium radius is unstable, as for slightly larger radius the constant outward velocity term leads to growth of the LSs while for slightly smaller radii curvature dominates and circular LSs shrink.

As the control parameter is changed away from p_M, the nucleation radius is reduced until the tail interactions become of comparable importance, leading to the typical snaking behaviour of the solution branch. Note that depending on the relative importance of the tail interaction and the curvature, the LSs may or may not extend all the way to p_M. Typically, γ is large, however, and the curvature has to be partially compensated by an outward velocity due to the relative stability of the two homogeneous solutions before the tail interactions stabilize the LSs. This is the case in Figs 2 and 3.

The interpretation of this collapse in the spatial dynamics picture is now necessarily different from that in the 1D case. A tangency between the stable and unstable manifolds of both fixed points must still occur at p_M with $R_0 \to \infty$ but because the vector field is now non-autonomous there are no associated homoclinics. Thus, the heteroclinic does not oscillate as it approaches the domain center. Away from p_M, the heteroclinic turns continuously into a homoclinic. Further out there is a regime crossover and spatial oscillations induce further crossings of the stable and unstable manifolds of the fixed point at infinity (cf. Lloyd & Sandstede, 2009), creating new localized states with small radius via saddle-node bifurcations, leading to the observed characteristic snaking.

This case has been studied in detail in the forced complex Ginzburg–Landau (FCGL1) equation with 1:1 temporal resonance (Ma & Knobloch, 2016):

$$A_t = (1 + i\alpha)\nabla^2 A + (\mu + i\nu)A - (1 + i\beta)|A|^2 A + p. \tag{3.2}$$

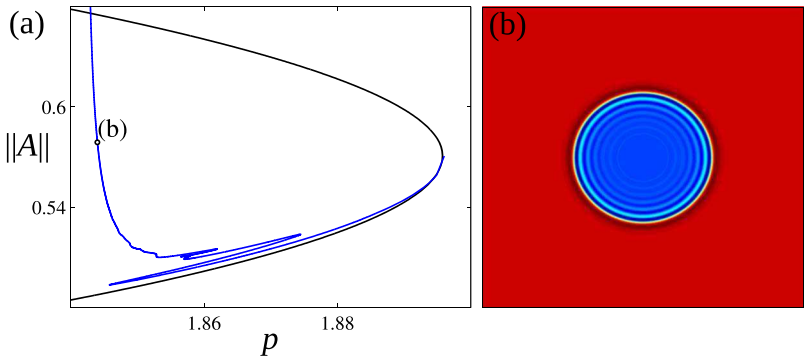

FIG. 3. Axisymmetric localized states in the FCGL1 equation (3.2). (a) Branch of steady axisymmetric states (blue line) followed from the lower right fold when $\nu = 5$ showing the transition from collapsed snaking to non-snaking, monotonic behaviour. (b) Sample solution profile $\mathrm{Im}[A(x, y)]$ at $p = 1.844$ in the monotonic regime, location as indicated in (a). Reprinted from Ma & Knobloch (2016), Copyright (2016), with permission from Elsevier.

Here $A(x, y, t)$ is a complex amplitude, ν represents the detuning between the natural frequency of the system and the frequency of the forcing and p is the strength of the forcing. The remaining parameters take the values $\mu = -1$, $\alpha = -1.5$, $\beta = 6$. For $\nu = 5$, this system exhibits bistability between two homogeneous states phase-locked to the drive. As usual, localized states bifurcate from the vicinity of the folds of these states, and this is so in both 1D and 2D. Figure 3 shows the collapsed snaking of an axisymmetric localized state that bifurcates from the lower right fold and the transition from collapsed snaking to the predicted monotonic approach to the Maxwell point, together with a sample solution profile in the latter regime.

3.3 *Collapsed radial snaking of circular fronts between equivalent states*

In the case of equivalent states ($c_0 = a = 0$), the dynamics of large circular domains is determined by curvature terms only, but for small radii the tail interactions come into play and may lead to stationary LSs with a small radius, much as in the previous case. If the coefficient γ is too large as compared to the tail interaction strength g, curvature may prevent the formation of LSs altogether. For $p \simeq p_c$, however, γ takes very small values and LSs can form. Moreover, around that point nonlinear curvature effects have to be taken into account. Nonlinear curvature effects and tail interactions allow then for the formation of two distinct types of stationary radially symmetric LSs belonging to the same homoclinic snaking curve (Fig. 4). If $b < 0$ and for large R, nonlinear curvature effects counteract the linear contribution creating stable large-radius localized states, named stable droplets (SDs), as described by Gomila *et al.* (2001). The equilibrium radius is given by

$$R_0 = \sqrt{\frac{-b}{\gamma_0}} \frac{1}{\sqrt{p - p_c}}. \tag{3.3}$$

The branch of SDs does not snake when approaching p_c, but the scaling of the collapse differs from the previous case. Here the change of sign of the coefficient γ plays a similar role to the 'Maxwell point' in the previous two cases.

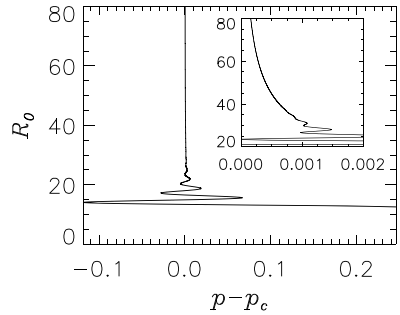

FIG. 4. Stationary radius R_0 of stable droplets (SDs) as a function of p according (2.7). The inset shows the crossover region where the equilibrium radius goes from being determined by the interaction of the oscillatory tails of the profile to being dominated by nonlinear curvature effects. Here $c = 0$, $\gamma_0 = 1$, $a = 0$, $b = -1$, $g = 10$, $\beta = 1$ and $\alpha = -0.25$.

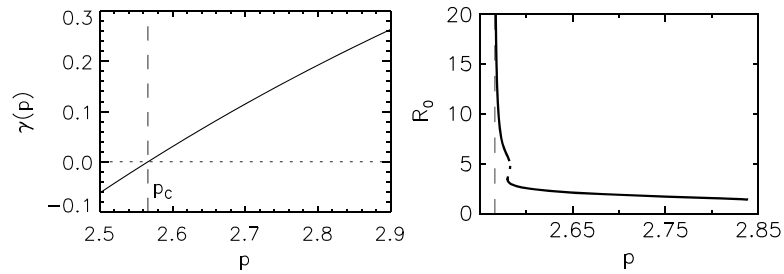

FIG. 5. Dependence of the surface tension γ (left) and equilibrium radius R_0 (right) on the amplitude p of the forcing in FCGL2. The bifurcation diagram on the right shows the predicted transition from collapsed snaking to monotonic behaviour; the solid (dashed) lines indicate stable (unstable) solutions. Here $\alpha = 2$, $\beta = 0$, $\mu = 0$ and $\nu = 2$. For these values of the parameters $p_c = 2.56629$.

For smaller radii, tail interaction prevails over nonlinear curvature effects leading to characteristic snaking in the LS bifurcation diagram. As usual, sections with positive (negative) slopes correspond to stable (unstable) LSs.

This scenario is quite general and applies to 2D systems displaying bistability between two equivalent homogeneous solutions, i.e. states arising from a pitchfork bifurcation, and has been studied theoretically, for instance, in the forced complex Ginzburg–Landau (FCGL2) equation with 2:1 temporal resonance (Gomila *et al.*, 2001):

$$A_t = (1 + i\alpha)\nabla^2 A + (\mu + i\nu)A - (1 + i\beta)|A|^2 A + pA^*. \tag{3.4}$$

This system exhibits bistability between two equivalent homogeneous states phase-locked to the driving with a π phase difference. Figure 5 shows the dependence of the surface tension γ on the control parameter p and the corresponding equilibrium radius R_0 of circular LSs in the FCGL2, while Fig. 6 shows examples of LSs and SDs in the FCGL2. In Fig. 6, the right panels show the radial spatial trajectory of LS and SD in phase space. Note that the smaller the radius the larger the departure from the heteroclinic trajectory corresponding to the flat front.

The same behaviour has been observed in the mean field equations for a self-defocusing Kerr resonator and in degenerate optical parametric oscillators (DOPOs) (Gomila *et al.*, 2003). Figure 7

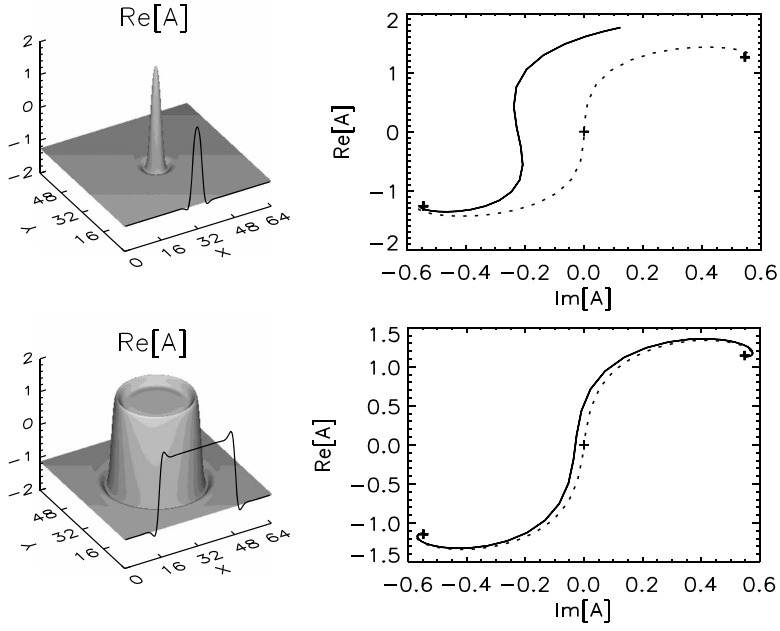

FIG. 6. Localized state (top) for $p = 2.7$ and stable droplet (bottom) for $p = 2.569$ in FCGL2. Left: 3D rendering and transverse section of LS and SD (black line). Right: plot of Im[A] against Re[A] along the radial coordinate. The dotted curve shows the corresponding 1D front for comparison.

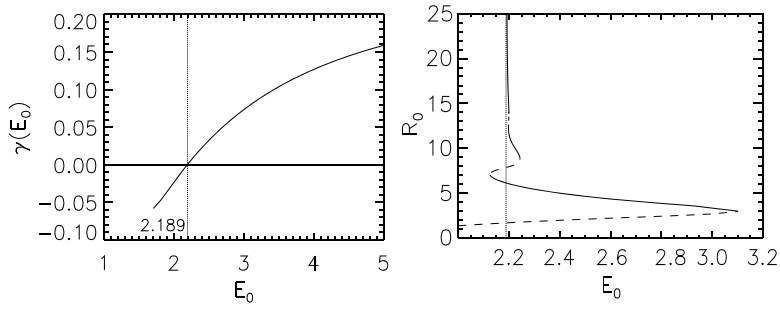

FIG. 7. Dependence of the surface tension γ (left) and equilibrium radius R_0 (right) on the amplitude E_0 of the external pump field in DOPO. The bifurcation diagram on the right shows the predicted transition from collapsed snaking to monotonic behaviour; the solid (dashed) lines indicate stable (unstable) solutions.

shows the dependence of the surface tension γ on the amplitude of the input field E_0 and the corresponding equilibrium radius R_0 of circular LSs in the DOPO.

Experimental evidence of this type of behaviour has been found in a nonlinear optical system consisting of a sodium vapour cell with a single-mirror feedback (Pesch *et al.*, 2007), although in that experiment the condition $\gamma = 0$ was not in an experimentally accessible parameter range. The change of sign of the γ coefficient has, however, been observed in a temporally forced bistable oscillatory

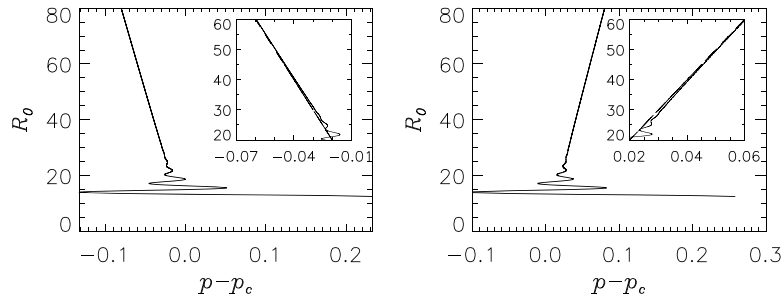

FIG. 8. Stationary radius R_0 as a function of p according (2.7) for $c < 0$ (left) and $c > 0$ (right). The inset shows the transition from LS to the nucleation radius with a linear dependence on p. The slanted straight line indicates the nucleation radius according (3.5). Here $c = \pm 0.001$, $\gamma_0 = 1$, $b = -1$, $g = 10$, $\beta = 1$ and $\alpha = -0.25$.

Belousov–Zhabotinsky chemical reaction (Marts *et al.*, 2004), where both growing and shrinking high curvature fronts were observed upon changing the frequency of the forcing.

3.4 *Slanted radial collapsed snaking*

In systems with two non-equivalent states, the velocity c is in general non-zero and vanishes only at the 'Maxwell point' ($p = p_M$). Away from this point and close to p_c, one can consider c to be constant and O(1) for small changes of p. In this case, the LS bifurcation diagram is similar to the previous case but slanted towards larger or smaller values of p depending on the sign of c (Fig. 8). For $c \neq 0$, nonlinear curvature effects do not play a crucial role and the large stationary radius corresponds to the nucleation radius, where the inwards or outwards velocity due to the relative stability of the homogeneous solutions is balanced by the curvature:

$$R_0 = \frac{\gamma_0}{c}(p - p_c)\,. \tag{3.5}$$

If $c > 0$, meaning that the inner solution overruns the outer solution, a stationary radius exists for positive γ, i.e. $p > p_c$. If $c < 0$, the opposite is the case. In both cases, the nucleation radius is unstable, although for different reasons. When $c > 0$, the stationary radius is unstable, as increasing R leads to a decrease in the inward force and the circular domain therefore expands forever. On the other hand, decreasing R leads to the opposite behaviour and the circular LS shrinks. In contrast, if $c < 0$, the nucleation radius is radially stable, but as γ is then negative, the interface is modulationaly unstable leading to the formation of labyrinthine patterns (Gomila *et al.*, 2001, 2004). Close to p_c γ is always small enough for the oscillatory tails to lead to small-radius LSs.

Such behaviour has been studied in FCGL2 with a constant term ϵ breaking the symmetry between the two homogeneous solutions (Gomila *et al.*, 2004). The velocity c of a 1D front is then proportional to ϵ. Figure 9 shows the bifurcation diagram of localized states in asymmetric FCGL2 for positive and negative ϵ.

4. Localized states with internal structure

It is tempting to think that the notion of an effective surface tension applies quite generally and that it helps explain the existence of all localized states in 2D. However, this appears not to be the case.

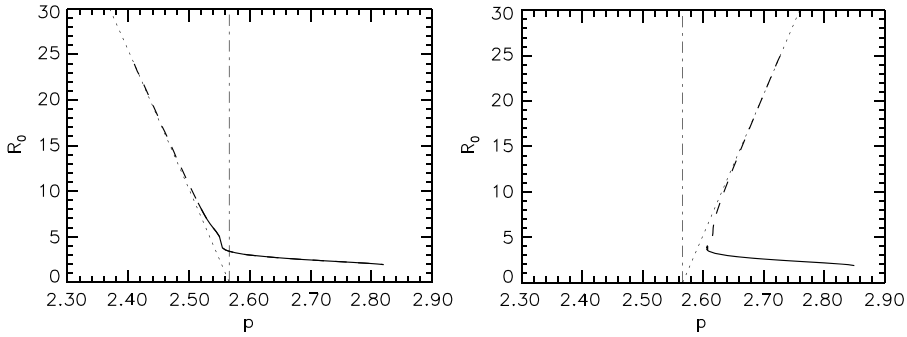

FIG. 9. Dependence of the stationary radius R_0 on the amplitude p of the forcing in the asymmetric FCGL2 for $\epsilon < 0$ (left) and $\epsilon > 0$ (right). Solid (dashed) lines indicate stable (unstable) solutions. The dotted straight line indicates the nucleation radius according to (3.5). Parameters are as in Fig. 5 with $\epsilon = \pm 0.05$.

The simplest localized states in 2D with internal structures are axisymmetric states such as those studied by Lloyd & Sandstede (2009) and McCalla & Sandstede (2010). In particular, in the latter work, McCalla and Sandstede carry out extensive numerical continuation of axisymmetric states in the quadratic-cubic Swift–Hohenberg equation starting from small amplitude states referred to as Spot A and Spot B. Associated with these are structures referred to as Ring A and Ring B. Spots A and B differ in whether they have a maximum or a minimum at $r = 0$ with a similar distinction between the ring states whose envelope peaks away from $r = 0$, however. The computations show that with increasing norm (i.e. larger radius of the localized state) the snaking structure emerging from Spot B connects with the corresponding structure arising from Ring B, thereby breaking up the structure into a stack of isolas. At yet larger amplitude these isolas reconnect again, forming a disconnected snaking structure that extends to infinite norm in both directions. Similar structures associated with Spot A and Ring A also reconnect but do not break up into isolas (McCalla & Sandstede, 2010). This intricate behaviour cannot be captured by the techniques described in the preceding section which are based on an expansion procedure valid in the limit of small curvature. These techniques, suitably modified by the inclusion of the pinning effect (cf. (2.7) but with $\alpha = 0$) should, however, be able to capture the snaking properties of large axisymmetric structures, i.e. those present beyond the isola states. It is important to realize that the steady state problem in the radial coordinate r is non-autonomous, a fact that is responsible in finite domains for the observed continuous transition from small amplitude spot states to radially confined rings and ultimately to domain-filling target states. This is in contrast to the corresponding behaviour on a periodic domain in 1D (Burke & Knobloch, 2007) where LS are created in a secondary bifurcation from a small amplitude periodic state and destroyed in another secondary bifurcation near the fold of the latter. We mention that in finite but large circular domains these snaking structures interact with analogous states confined to the domain boundary, leading to yet more complex behaviour (Verschueren *et al.*, 2021).

Additional issues arise when one considers non-axisymmetric structures. In Figs. 10 and 11, we show two stationary 2D structures found in the cubic-quintic Swift–Hohenberg equation (Avitabile *et al.*, 2010). Both snake as one might expect from a system with a preferred intrinsic wavenumber, a fact that distinguishes the Swift–Hohenberg equation from the Ginzburg–Landau equation considered thus far.

The barrel-shaped structure shown in Fig. 10 presents an example of the role played by the intrinsic wavenumber. The straight fronts on either side of the structure are pinned to the oscillations behind

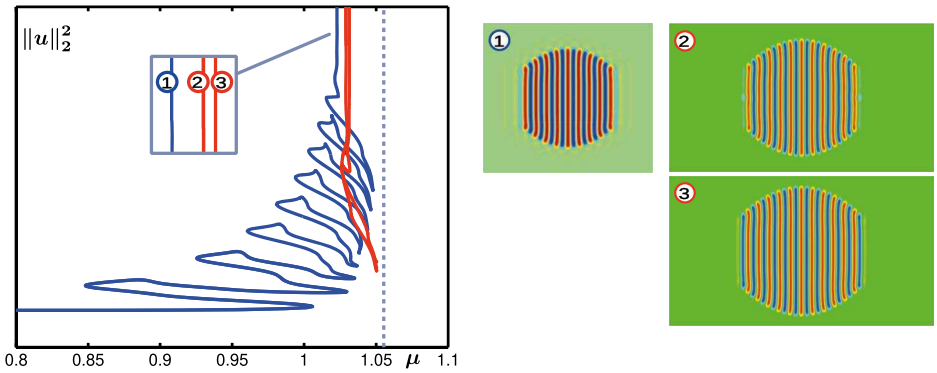

FIG. 10. Time-independent barrel states of the subcritical cubic-quintic Swift–Hohenberg equation. The left panel contains two disjoint branches of fully localized planar stripe patterns and shows the Maxwell point $\mu_M = 1.0560$ of 1D stripes as a vertical dashed line. The blue curve corresponds to barrel states with 9 stripes (panel 1) and approaches the vertical asymptote $\mu = 1.0228$. The red curve corresponds to states with 11 stripes (panels 2 and 3): its limiting asymptotes are $\mu = 1.0290$ and $\mu = 1.0314$. The red curve has been rescaled linearly in the vertical direction to fit on the same graph. For additional details, see Avitabile *et al.* (2010). Copyright ©2010 Society for Industrial and Applied Mathematics. Reprinted with permission. All rights reserved.

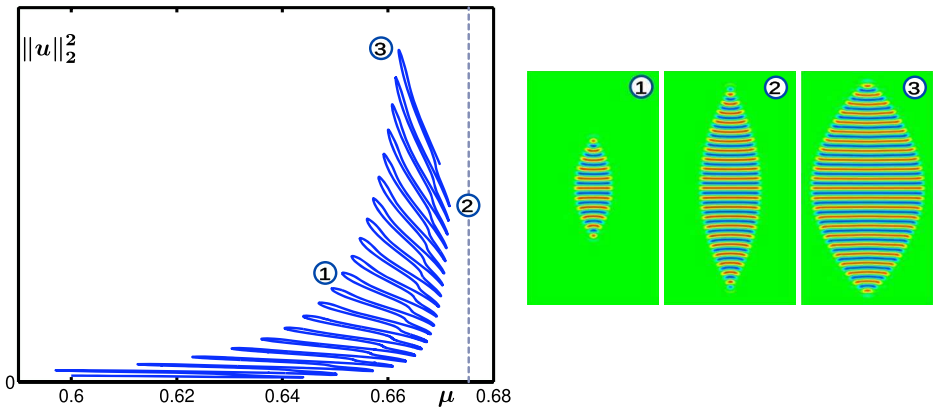

FIG. 11. Time-independent worm states of the subcritical cubic-quintic Swift–Hohenberg equation. The Maxwell point of 1D stripes occurs at $\mu = 0.6753$ (vertical dashed line). For additional details, see Avitabile *et al.* (2010). Copyright ©2010 Society for Industrial and Applied Mathematics. Reprinted with permission. All rights reserved.

them, thereby explaining why the structure does not expand in the x direction. It is less clear why it does not expand in the perpendicular or y direction: if one cuts off the regions that bow out, the straight fronts that result will see a homogeneous state behind them and hence no pinning will take place and the fronts will travel in the y direction whenever the parameters depart from the Maxwell point, i.e. for all but isolated parameter values. In this case, one might expect that the structure will grow into a state extended in the y direction, with vertically extended stripes in the interior. States of this type are a trivial extension of 1D states into 2D and their stability properties were studied by Burke & Knobloch (2006), where it was shown that instabilities of the lateral fronts via the so-called wall modes, coupled with possible interior or bulk instabilities, both serve to reduce the pinning region where states of this type are stable. In fact, because of differential growth due to the presence of corners in the initial

condition, the state does not evolve into such a localized stripe pattern and instead forms a growing worm (Lloyd, 2019).

It follows that the bowed or curved fronts in Fig. 10 are stationary for another reason and we conjecture that this is due to a combination of the pinning that arises from the wavenumber gradient normal to the curved front, i.e. from the fact that the wavenumber along the front is smaller than that in the interior of the structure, and the curvature-driven behaviour of the previous section. In particular, we believe that the pinning effect just described affects the surface tension due to the front curvature and that the two together determine the effective surface tension that holds the structure together.

Figure 11 shows the more extreme example of a so-called worm state. These states also exhibit stationary bowed or curved fronts that hold the structure together, and the confining mechanism is likely the same. Here, however, one finds that while the fronts are in general convex, close to the tips they become in some cases concave (panel 2). This may be because of the sharp tip (which cannot represent a singularity of the equations, however) but it does imply that the pinning and curvature effects are not purely additive. In particular, the notion of surface tension is a property of the envelope of the front, and it breaks down as soon as the front acquires spatial structure comparable to its width, as is the case near the tip of these worm structures. These questions merit further study.

The intrinsic wavenumber also plays a role in the depinning process that takes place outside the snaking or pinning region where no stationary localized states are present. In 1D, one finds that the LSs either grow (beyond the right boundary of the pinning region) or shrink (below the left boundary of the pinning region), as exemplified by the 1D Swift–Hohenberg equation (Burke & Knobloch, 2006). In this case, the structures grow (shrink) by nucleating new (suppressing old) wavelengths on either side of the structure, while its interior remains at rest. However, this is not the only way that LSs grow after depinning.

The FCGL1 equation (3.2) provides an example of the new behaviour. In this system, one finds a distinct growth mechanism whereby the LS grows from the middle. Here the middle cell splits into two which are then ‘pushed’ aside while a new cell regrows in the middle. Thus, the two halves of the structure are continuously pushed aside. Note that in this case the structure grows as a result of a phase slip that takes place in the center and that the growth of the structure is a consequence of repeated phase slips, in contrast to the growth of LSs in the 1D Swift–Hohenberg equation which does not require or depend on phase slips (Ma & Knobloch, 2012). When the structure is large enough the preferred location of the phase slips shifts from the center of the structure to a pair of locations, one on either side, where new cells continue to be injected, as required by the presence of a preferred wavenumber. Ma & Knobloch (2012) show some examples of this behaviour which remains poorly understood. Note that for full understanding one needs to have a theory of the Eckhaus instability for time-dependent patterns, and incorporate the fact that the Eckhaus instability that triggers phase slips sets in through a delayed bifurcation (Knobloch & Krechetnikov, 2014).

In 2D, similar behaviour is found. Figure 12 shows that target states exhibit a more complex form of snaking that resembles the collapsed snaking in Fig. 3 but no longer collapses to a point. This is a consequence of the internal structure which pins the circular front to the structure within. Moreover, and in contrast to the 1D case, the asymptotic location of the folds converges algebraically, as observed already by McCalla & Sandstede (2010) for the Swift–Hohenberg equation. Outside this pinning region axisymmetric states depin and the structure either grows or shrinks, as shown in Fig. 13. Depending on parameters, one sees that the structure may shrink via phase slips in the center or via additional phase slips on either side of the center, just as in the 1D case.

The above results were obtained by imposing axisymmetry on the structure. If this constraint is relaxed, however, the target pattern breaks up into hexagons, the preferred state of a Turing-unstable

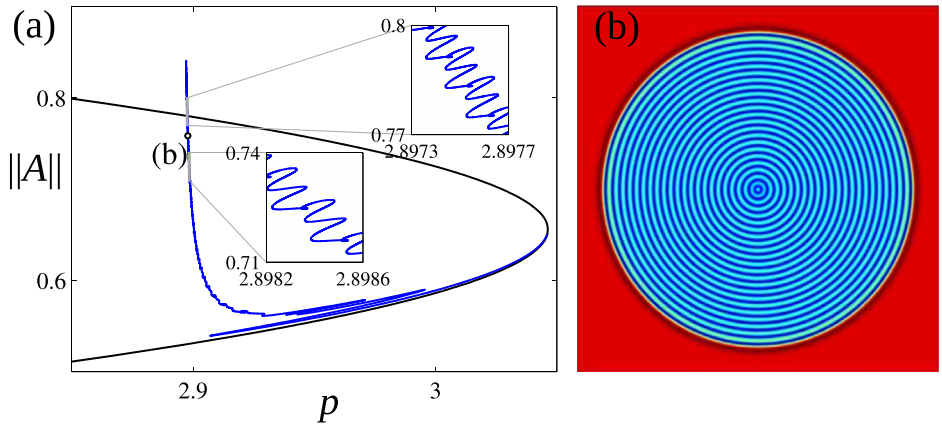

FIG. 12. Localized target states in the FCGL1 equation (3.2) when $\nu = 7$. (a) The branch of steady axisymmetric target states followed from the lower right fold snakes but does not become monotonic. (b) Sample solution profile Im$[A(x, y)]$ at the location indicated in (a). Reprinted from Ma & Knobloch (2016), Copyright (2016), with permission from Elsevier.

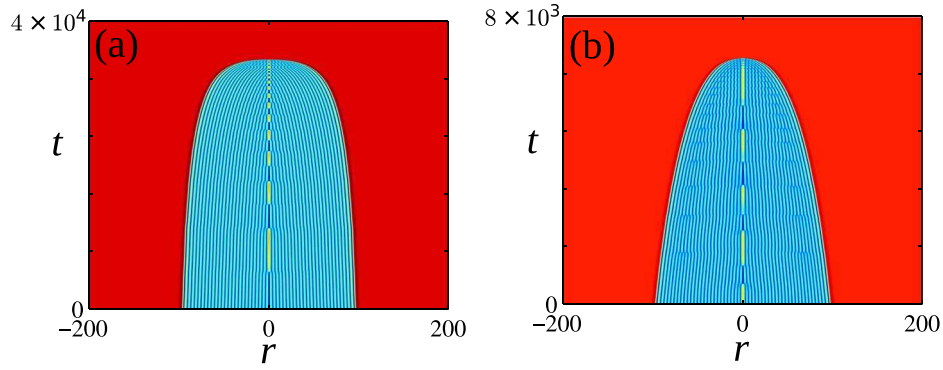

FIG. 13. Collapsing localized states in the axisymmetric FCGL1 equation (3.2) showing the transition from (a) on-center phase slips to (b) additional off-center phase slips. In each case, the plot has been reflected in $r = 0$ to obtain a complete cross-section. Reprinted from Ma & Knobloch (2016), Copyright (2016), with permission from Elsevier.

homogeneous state in this system (Fig. 14). However, a hexagonal pattern does not fit into the interior of a circular front, inevitably leading to spatial modulation of the pattern close to the boundary. This geometrical mismatch in turn triggers Eckhaus instabilities which inject new cells in the interior or that annihilate existing cells. These phase slips occur intermittently and in different locations in the interior leading to irregular evolution of the radius of the structure. Different outcomes are possible. If the parameters are far from the 'Maxwell point' the evolution of the radius is primarily 'energy' driven, with phase slips occurring as required to maintain an approximately constant wavenumber in the interior as the radius of the structure increases (or decreases). However, a particularly interesting situation arises close to the 'Maxwell point'. Here the growth of the structure, i.e. the motion of the circular front, no longer relies on an 'energy' difference (equivalently, distance from a 'Maxwell point') between the two competing states (the homogeneous state and the hexagonal Turing state) and is instead the result of persistent 'random' phase slips in the interior as the cells inside try to (but are unable to) adjust to the

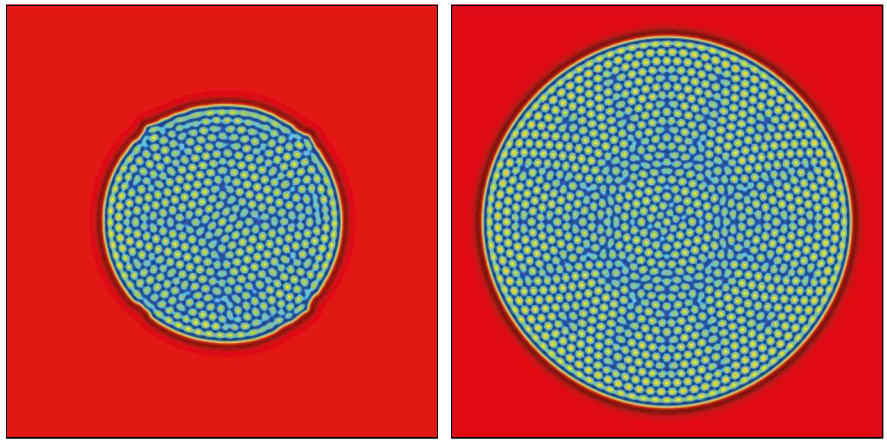

FIG. 14. Snapshots of LSs in the FCGL1 equation (3.2) in 2D showing $\mathrm{Im}[A(x,y)]$ for $\nu = 7$ and (a) $p = 2.8978$ and (b) $p = 2.8989$. Reprinted from Ma & Knobloch (2016), Copyright (2016), with permission from Elsevier.

constraint imposed by the circular boundary (Ma & Knobloch, 2016). The resulting long time evolution of the circular front resembles a random walk but remains to be studied.

For all the examples shown in this section, the usefulness of the notion of surface tension as a physically motivated mechanism responsible for radial confinement remains an open question. This is fundamentally a consequence of the fact that the systems examined above are open systems. In closed systems, the notion of surface tension can be defined more precisely and surface tension is indeed found to play a significant role in axisymmetric structures (drops and bubbles). As explained in greater detail by Thiele *et al.* (2019), this is so even when the system is finite, i.e. away from the thermodynamic limit.

5. Conclusions

We have reviewed the dynamics of circular fronts between two homogeneous solutions. We have explained in what sense the bifurcation diagrams of axisymmetric localized states both resemble and differ from the collapsed homoclinic snaking familiar from 1D systems. First, in systems with two non-equivalent homogeneous solutions the scenario resembles that familiar from the 1D case, but the snaking collapses algebraically, with $R_0 \propto 1/|p-p_M|$ asymptotically close to the Maxwell point, instead of exponentially, and no snaking takes place asymptotically. The asymptotic equilibrium radius R_0 then corresponds to the so-called nucleation radius in phase decomposition.

In cases where the system has a symmetry that relates the two competing homogeneous states, the collapse of the snaking curve is determined by curvature effects and not the 'Maxwell point' between the competing states. The bifurcation curve then collapses to the critical point where γ, the 'surface tension' that determines the strength of the curvature-driven dynamics, vanishes. Very close to this point, stationary states with large radius (SDs) correspond to an equilibrium between linear and nonlinear curvature terms. In this case, the bifurcation curve approaches the vertical asymptote monotonically, with $R_0 \propto 1/|p-p_c|^{1/2}$, and no snaking takes place. For smaller radii, the interaction between oscillatory tails comes into play, introducing oscillations in the bifurcation diagram characteristic of homoclinic snaking. This indicates that, despite the equivalence of the two competing states, the radial spatial

dynamics formulation admits a heteroclinic connection between the corresponding fixed points but does so at $p = p_c$ only (collapsed snaking).

In systems with two non-equivalent homogeneous states far from the Maxwell point the scenario remains similar, but the associated bifurcation diagram becomes slanted. The asymptote for the large radius equilibrium state corresponds to a nucleation radius where the curvature is balanced by the constant velocity of the 1D front. In this case, $R_0 \propto |p - p_c|$. Such states are always unstable, radially for positive c and positive γ, and azimuthally for negative c and negative γ, as the latter induces modulational instability of the front, leading to labyrinthine structures.

We have also examined the effects of the curvature on LSs with internal structure. Here the situation is less clear since surface tension now competes with pinning. For this reason, it is essential to distinguish between axisymmetric structures in which the local wavevector points radially and pinning is strong, and structures in which the local wavevector is almost parallel to the front, with weaker pinning effects as a result. In general, curvature and pinning act on different scales, with pinning effects occurring at smaller scales, beyond the validity of effective eikonal equations for the front envelope but this may not be the case for the worm states in Fig. 11. In contrast, we have seen that axisymmetric states continue to snake in the asymptotic limit of large R but that the approach of the folds to the boundary of the snaking interval is now algebraic and not exponential, thereby combining the key characteristics of both homoclinic and collapsed snaking. The depinning of circular LSs with internal structure also shows unusual behaviour that highlights the importance of phase slips in the interior of the structure and suggests that persistent phase-slip driven front propagation is a distinct possibility.

While we have presented evidence for collapsed radial snaking and discussed some of its characteristics, a rigorous description of this behaviour in terms of radial spatial dynamics is lacking. The different regimes and scaling behaviour described in this work must be organized by the codimension-2 point $p_M = p_c$, whose universal unfolding remains an open question. We hope some of the ideas presented here will help in the development of a rigorous mathematical theory for collapsed radial snaking.

Funding

FEDER/Ministerio de Ciencia, Innovación y Universidades—Agencia Estatal de Investigación/ SuMaEco (RTI2018-095441-B-C22 to D.G.); National Science Foundation (DMS-1908891 to E.K.).

References

Akhmediev, N. & Ankiewicz, A. (eds.) (2008) *Dissipative Solitons: From Optics to Biology and Medicine*. Lecture Notes in Physics, vol. 751. Berlin: Springer, pp. 1–492.

Allen, S. M. & Cahn, J. W. (1979) A microscopic theory for antiphase boundary motion and its application to antiphase domain coarsening. *Acta Metall. Mater.*, **27**, 1085–1095.

Avitabile, D., Lloyd, D. J. B., Burke, J., Knobloch, E. & Sandstede, B. (2010) To snake or not to snake in the planar Swift–Hohenberg equation. *SIAM J. Appl. Dyn. Syst.*, **9**, 704–733.

Bramburger, J. J., Altschuler, D., Avery, C. I., Sangsawang, T., Beck, M., Carter, P. & Sandstede, B. (2019) Localized radial roll patterns in higher space dimensions. *SIAM J. Appl. Dyn. Syst.*, **18**, 1420–1453.

Burke, J. & Knobloch, E. (2006) Localized states in the generalized Swift–Hohenberg equation. *Phys. Rev. E*, **73**, 056211.

Burke, J. & Knobloch, E. (2007) Homoclinic snaking: structure and stability. *Chaos*, **17**, 037102.

Coullet, P., Elphick, C. & Repaux, D. (1987) Nature of spatial chaos. *Phys. Rev. Lett.*, **58**, 431–434.

Coullet, P., Riera, C. & Tresser, C. (2000) Stable static localized structures in one dimension. *Phys. Rev. Lett.*, **84**, 3069–3072.

Faye, G., Rankin, J. & Lloyd, D. J. B. (2013) Localized radial bumps of a neural field equation on the Euclidean plane and the Poincaré disc. *Nonlinearity*, **26**, 437–478.

Fernandez-Oto, C., Clerc, M. G., Escaff, D. & Tlidi, M. (2013) Strong non-local coupling stabilizes localized structures: an analysis based on front dynamics. *Phys. Rev. Lett.*, **110**, 174101.

Gallego, R., San Miguel, M. & Toral, R. (2000) Self-similar domain growth, localized structures, and labyrinthine patterns in vectorial Kerr resonators. *Phys. Rev. E*, **61**, 2241–2244.

Gelens, L., Gomila, D., Van der Sande, G., Matías, M. A. & Colet, P. (2010) Nonlocality-induced front interaction enhancement. *Phys. Rev. Lett.*, **104**, 154101.

Glasner, K. B. & Lindsay, A. E. (2013) The stability and evolution of curved domains arising from one-dimensional localized patterns. *SIAM J. Appl. Dyn. Syst.*, **12**, 650–673.

Gomila, D., Colet, P., Oppo, G.-L. & San Miguel, M. (2001) Stable droplets and growth laws close to the modulational instability of a domain wall. *Phys. Rev. Lett.*, **87**, 194101.

Gomila, D., Colet, P., San Miguel, M., Scroggie, A. J. & Oppo, G.-L. (2003) Stable droplets and dark-ring cavity solitons in nonlinear optical devices. *J. Quantum Electron.*, **39**, 238–244.

Gomila, D., Colet, P., Oppo, G.-L. & San Miguel, M. (2004) Stable droplets and nucleation in asymmetric bistable nonlinear optical systems. *J. Opt. B Quantum Semiclass. Opt.*, **6**, S265–S270.

Knobloch, E. & Krechetnikov, R. (2014) Stability on time-dependent domains. *J. Nonlin. Sci.*, **24**, 493–523.

Lewis, E. R. (2006) The effect of surface tension (Kelvin effect) on the equilibrium radius of a hygroscopic aqueous aerosol particle. *J. Aerosol Sci.*, **37**, 1605–1617.

Li, Z., Xu, Y., Coen, S., Murdoch, S. G. & Erkintalo, M. (2020) Experimental observations of bright dissipative cavity solitons and their collapsed snaking in a Kerr resonator with normal dispersion driving. *Optica*, **7**, 1195–1203.

Lloyd, D. J. B. (2019) Invasion fronts outside the homoclinic snaking region in the planar Swift–Hohenberg equation. *SIAM J. Appl. Dyn. Syst.*, **18**, 1892–1933.

Lloyd, D. & Sandstede, B. (2009) Localized radial solutions of the Swift–Hohenberg equation. *Nonlinearity*, **22**, 485–524.

Lo Jacono, D., Bergeon, A. & Knobloch, E. (2017) Spatially localized radiating diffusion flames. *Combust. Flame*, **176**, 117–124.

Ma, Y.-P. & Knobloch, E. (2012) Depinning, front motion, and phase slips. *Chaos*, **22**, 033101.

Ma, Y.-P. & Knobloch, E. (2016) Two-dimensional localized structures in harmonically forced oscillatory systems. *Phys. D*, **337**, 1–17.

Marts, B., Martinez, K. & Lin, A. L. (2004) Front dynamics in an oscillatory bistable Belousov–Zhabotinsky chemical reaction. *Phys. Rev. E*, **70**, 056223.

McCalla, S. & Sandstede, B. (2010) Snaking of radial solutions of the multi-dimensional Swift–Hohenberg equation: a numerical study. *Phys. D*, **239**, 1581–1592.

Meron, E. (1992) Pattern formation in excitable media. *Phys. Rep.*, **218**, 1–66.

Ophaus, L., Knobloch, E., Gurevich, S. V. & Thiele, U. (2021) Two-dimensional localized states in an active phase-field-crystal model. *Phys. Rev. E*, **103**. 032601.

Oppo, G.-L., Scroggie, A. J. & Firth, W. J. (1999) From domain walls to localized structures in degenerate optical parametric oscillators. *J. Opt. B*, **1**, 133–138.

Oppo, G.-L., Scroggie, A. J. & Firth, W. J. (2001) Characterization, dynamics and stabilization of diffractive domain walls and dark-ring cavity solitons in parametric oscillators. *Phys. Rev. E*, **63**, 066209.

Ouchi, K. & Fujisaka, H. (1996) Phase ordering kinetics in the Swift–Hohenberg equation. *Phys. Rev. E*, **54**, 3895–3898.

Oza, A. U., Harris, D. M., Rosales, R. R. & Bush, J. W. M. (2014) Pilot-wave dynamics in a rotating frame: On the emergence of orbital quantization. *J. Fluid Mech.*, **744**, 404–429.

Parra-Rivas, P. & Fernandez-Oto, C. (2020) Formation of localized states in dryland vegetation: bifurcation structure and stability. *Phys. Rev. E*, **101**, 052214.

Parra-Rivas, P., Knobloch, E., Gelens, L. & Gomila, D. (2020) Origin, bifurcation structure and stability of localized states in Kerr dispersive optical cavities (this issue). arXiv: 2010.03375.

Perez, M. (2005) Gibbs–Thomson effects in phase transformations. *Scr. Mater.*, **52**, 709–712.
Pesch, M., Lange, W., Gomila, D., Ackemann, T., Firth, W. J. & Oppo, G.-L. (2007) Two-dimensional front dynamics and spatial solitons in a nonlinear optical system. *Phys. Rev. Lett.*, **99**, 153902.
Purwins, H.-G., Bödeker, H. U. & Amiranashvili, Sh. (2010) Dissipative solitons. *Adv. Phys.*, **59**, 485–701.
Shen, J. & Yang, X. (2010) Numerical approximation of the Allen–Cahn and Cahn–Hilliard equations. *Discrete Contin. Dyn. Sys.*, **59**, 485–701.
Staliunas, K. & Sanchez-Morcillo, V. J. (1998) Spatial-localized structures in degenerate optical parametric oscillators. *Phys. Rev. A*, **57**, 1454–1457.
Thiele, U., Frohoff-Hülsmann, T., Engelnkemper, S., Knobloch, E. & Archer, A. J. (2019) First order phase transitions and the thermodynamic limit. *New J. Phys.*, **21**, 123021.
Tseluiko, D., Galvagno, M. & Thiele, U. (2014) Collapsed heteroclinic snaking near a heteroclinic chain in dragged meniscus problems. *Eur. Phys. J. E*, **37**, 33.
Tzou, J. C., Ma, Y.-P., Bayliss, A., Matkowsky, B. J. & Volpert, V. A. (2013) Homoclinic snaking near a codimension-two Turing–Hopf bifurcation point in the Brusselator model. *Phys. Rev. E*, **87**, 022908.
Verschueren, N., Knobloch, E. & Uecker, H. (2021) Localized and extended patterns in the cubic-quintic Swift–Hohenberg equation on a finite disk. *Phys. Rev. E* (in press). arXiv: 2104.05852.
Woods, P. D. & Champneys, A. R. (1999) Heteroclinic tangles and homoclinic snaking in the unfolding of a degenerate reversible Hamiltonian–Hopf bifurcation. *Phys. D*, **129**, 147–170.